Article

An Easy Method of Synthesis Co_xO_y@C Composite with Enhanced Microwave Absorption Performance

Wenli Bao [1,*,†], Cong Chen [1,2,†] and Zhenjun Si [1,*]

[1]   School of Materials Science and Engineering, Changchun University of Science and Technology, No. 7989, Weixing Road, Changchun 130022, China; cccmcx@163.com

[2]   School of Physics and Electronic Information Engineering, Qinghai Nationalities University, Xining 810007, China

*   Correspondence: zdbwl@163.com (W.B.); szj@cust.edu.cn (Z.S.)

†   The first two authors contributed equally to this paper.

check for updates

Abstract: Design of interface-controllable magnetic composite towards the wideband microwave absorber is greatly significance, however, it still remains challenging. Herein, we designed a spherical-like hybrids, using the Co_3O_4 and amorphous carbon as the core and shell, respectively. Then, the existed Co_3O_4 core could be totally reduced by the carbon shell, thus in Co_xO_y core (composed by Co and Co_3O_4). Of particular note, the ratios of Co and Co_3O_4 can be linearly tuned, suggesting the controlled interfaces, which greatly influences the interface loss behavior and electromagnetic absorption performance. The results revealed that the minimum reflection loss value (RL_{min}) of −39.4 dB could be achieved for the optimal Co_xO_y@C sample under a thin thickness of 1.4 mm. More importantly, the frequency region with $RL < -10$ dB was estimated to be 4.3 GHz, ranging from 13.7 to 18.0 GHz. The superior wideband microwave absorption performance was primarily attributed to the multiple interfacial polarization and matched impedance matching ability.

Keywords: controllable interfaces; magnetic Co_xO_y@C composite; width band EM absorption; interfacial polarization; tunable content

1. Introduction

With the rapid development of electronic devices, e.g., radar communications, wireless and local area network, etc., the electromagnetic (EM) pollutions are becoming serious, especially for regarding as "health killer" and for simultaneously disturbing normal operation of other precious devices [1–3]. In case to reduce electromagnetic pollution, more attempts have been paid on exploration of functional materials with the strong dielectric or magnetic loss ability, so that the EM waves can be converted into heats by these materials [4,5]. Commonly, the efficiency of conversion from EM to heats is termed as reflection loss (*RL*) value. As an ideal EM material, it is commonly requested to a width band absorption (frequency region with $RL < -10$ dB, noted that −10 dB is regarded as the commercial standard with a conversion efficiency of 90%) [6,7]. Meanwhile, a thin thickness is quite vital to reduce the weight of absorption layer [8]. Nowadays, it is widely believed that EM performance is primarily influenced by both component and nanostructure; thus the strategy of component/nanostructure has been a general way to develop EM absorber [9]. As a desirable candidate, magnetic hybrids have been widely investigated, because of their dual magnetic and dielectric loss ability [10,11]. E.g., Jia et al. employed an in situ growth route to prepare $Fe/ZnFe_2O_4$ hybrids, and the frequency region (f_s) was up to 6.2 GHz under a matched thickness of 1.5 mm [12]. Zhao and coworker utilized a facile polyol reduction approach to prepare Co/CoO composite, and reported that f_s value was 4.2 GHz under a thickness of 1.7 mm [13]. Li et al. combined magnetic FeCo with SiO_2 and polypyrrole; the measured

f_s was ~6.8 GHz with a thickness of 2.5 mm [14]. For these desirable f_s values, the synergistic effect between magnetic and dielectric loss played a key role on the EM attenuation ability. Besides, the improved complex permeability value (μ_r) was also benefited to the impedance matching behavior [15]. In this case, more EM waves could enter into the interior of EM absorption layer for the subsequent attenuation. For this purpose, magnetic components are always decorated with a series of high dielectric material, to realize improvement of impedance matching behavior. These EM absorbers, such as included Fe/graphene, FeCo/graphene, Fe_3O_4/Mexnes, and so on, showed the distinct enhancement performance as compared to the single components [16,17].

Expecting for components, absorber with various morphologies also would make a great influence on the performance. E.g., Xu et al., taking graphene hybrid as a case, observed that loading same component with different nanostructure (nanoparticle/nanosheet), the dielectric loss ability was changed [18]. They explained that the changed dielectric loss ability was caused by interfacial polarization effect, which was highly associated with nanostructure. On the basis of this finding, Cao et al. designed a multiple-interface hybrid (namely, *Co_3O_4@rGO/SiO_2*) and achieved a f_s value of 4.2 GHz (*covering the entire X band*) [19]. Similarly, Zhang et al. reported a Fe_3Si/SiC@SiO_2 absorber and got a f_s value of 5.4 GHz (*d*~2.4 mm) [20]. All these desirable results confirmed the contribution of interfacial polarization.

Inspired by these results, we prepared a core–shell structured EM absorber, using Co/Co_3O_4 as the cores. The magnetic loss behavior can be easily tuned by adjusting the content of Co. Initial, Co_3O_4 nanospheres are made by a hydrothermal route and then used as the source of magnetic Co. Afterward, the as-obtained Co_3O_4 was coated by amorphous carbon to induce carbon reduction. The temperature for carbon reduction played a key role on the final content of Co. The developed Co/Co_3O_4@C presented excellent wideband EM absorption performance.

2. Experimental

2.1. Preparation of Co_3O_4 Nanospheres

Co_3O_4 nanospheres were prepared by a hydrothermal and annealing process. Typically, 0.1 g PVP, Co(Ac)$_2$, and urea (~20 mg) were codissolved in a mixture solvent, containing EG (20 mL) and distilled water (20 mL) and maintain at pH = 13. The above solution was used for the hydrothermal reaction, which was heated at 140 °C for 6 h. Once cooled to room temperature, the precipitate was collected by centrifugation for two to three times with distilled water. Later, Co_3O_4 was obtained by directly heating the precipitate at 300 °C for 0.5 h. Argon gas (Ar) was used as the protective gas.

2.2. Synthesis of Co/Co_3O_4@C Hybrids

Typically, 0.1 g Co(OH)$_2$ nanosphere, 0.4 g phenolic resin, and 0.2 mL formaldehyde were added into solution (~60 mL distilled water) and stirred for 2 h. Then, the as-obtained precipitates were heated at 500, 600, and 700 °C under Ar atmosphere for 1 h with a slow ramping rate of 1 °C/min. The obtained products treated at 500, 600, and 700 °C were denoted as C-Co-500, C-Co-600, and C-Co-700, respectively.

2.3. Characterization

The composition and phase of samples were determined by an X-ray diffractometer (Bruker D8 ADVANCE X-ray diffractometer) in the range of 20–60°. Field emission scanning electron microscope (FESEM, JEOL JSM-6330F) and transmission electron microscope (TEM, JEOL 2100) were used to observe the morphologies of these specimens. The chemical valences of Co element were evaluated by an X-ray photoelectron spectroscopy (XPS, PHI 5000 VersaProbe systems). Raman spectrum (Jobin Yvon HR 800 confocal Raman system) was employed to detect the graphitization level of the amorphous carbon shell. The coercive force (*Hc*) and magnetization were recorded by a vibrating sample magnetometer (VSM, Lakeshore, model 7400 series) at room temperature. EM characteristics

were evaluated on basis of a coaxial-line theory. First, the composites used for the EM absorption measurement were prepared by mixing the CoxOy@C with paraffin wax in 50 wt%. Afterwards, a cylindrical-shaped sample (Φ_{in} = 3.04 mm, Φ_{out} = 7.0 mm) was made by hot pressing the mixture into a mold. The electromagnetic parameters were tested by the two-port vector network analyzer (Agilent E5071C). Finally, the reflection loss value was calculated based on following equations [21–23]:

$$Z_{in} = Z_o(\mu_r/\varepsilon_r)^{1/2}\tanh[j(2\pi fd(\mu_r\varepsilon_r)^{1/2}/c)] \tag{1}$$

$$RL(dB) = 20\log|(Z_{in} - Z_o)/(Z_{in} + Z_o)| \tag{2}$$

where Z_{in} is the input impedance of absorber, f relates to the frequency of electromagnetic wave, d represents the coating thickness of the absorber, while c is the light velocity. ε_r ($\varepsilon_r = \varepsilon' - j\varepsilon''$) and μ_r ($\mu_r = \mu' - j\mu''$) are the complex permittivity and permeability of the absorption layer.

3. Results and Discussion

The formation process of Co/Co$_3$O$_4$@C spherical-shaped hybrids are illustrated in Figure 1. First, the spherical-shaped Co(OH)$_2$ samples are fabricated by a hydrothermal route. Second, Co(OH)$_2$ is converted to Co$_3$O$_4$ via annealing products at 300 °C for 1 h (Figure S1). The diffraction peaks intensity of Co$_3$O$_4$ and Co(OH)$_2$ are very strong, which are due to the good crystalline structure. Co(OH)$_2$@ phenolic resin (PS: the precursor of amorphous carbon) is made by an in situ polymerization route. By heating the Co(OH)$_2$@PS at various temperatures (here is 500–700 °C), Co/Co$_3$O$_4$@C with various content of Co can be obtained. Figure S2 compares the EDS and FTIR spectra of Co(OH)2@PS and C-Co-500 sample. The EDS spectra of Co(OH)$_2$@PS and Co/Co$_3$O$_4$@C samples are provided in Figure S2a,b, where the C, Co, and O elements can be detected on both samples. Hence, it is hard to observe the changes of component. Subsequently, the FT-IR spectra have been added to compare the changes of chemical bonds (Figure S2c,d). Clearly, the wave number at around 575 cm^{-1} is assigned to the characteristic vibrating peak of Co(OH)$_2$ and is consistent with the XRD result. After heating at 500 °C, the C-OH peak disappeared and turned to two types of Co-O bonds, known as CoO$_4$ (550 cm^{-1}) and CoO$_6$ (670 cm^{-1}), suggesting the coexisted spinel phase of Co$_3$O$_4$. Additionally, due to the carbonized reaction, the original C-H bond disappeared for the C-Co-500 sample.
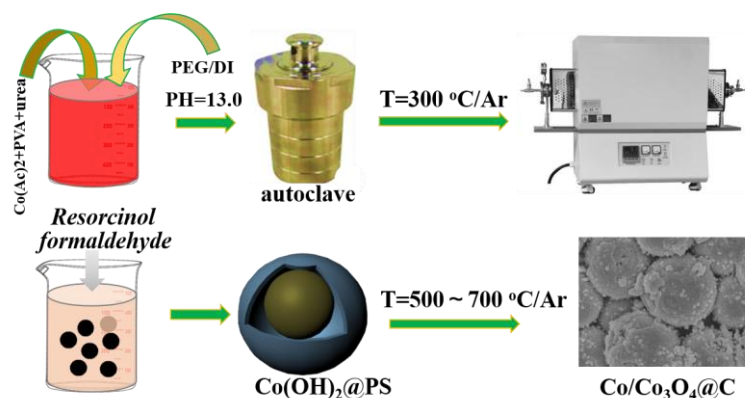

Figure 1. Schematic presentation for the preparation route of Co/Co$_3$O$_4$@C composites.

Figure 2 shows the morphology evolution from initial Co(OH)$_2$ to ultimate Co/Co$_3$O$_4$@C. Co(OH)$_2$ exhibits significant spherical-shaped structure with average size of ~400 nm (Figure 2a,b). The surface of Co(OH)$_2$ is very smooth and dense. As for Co$_3$O$_4$, it still maintains original spherical shape with the same size, according to Figure 2c,d. But Co$_3$O$_4$ exhibits a tiny rough surface attributing to the loss of phase conversion from Co(OH)$_2$ to Co$_3$O$_4$. Similarly, structure can be maintained for Co/Co$_3$O$_4$@C (C-Co-700), expecting for the surface (Figure 2e,f) to be rough, which was attributed to the amorphous carbon shell.

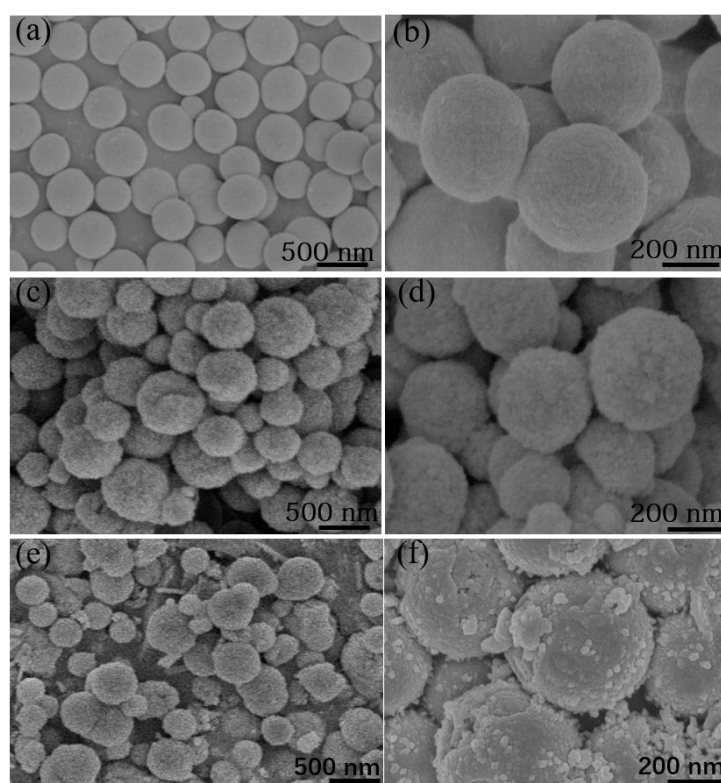**Figure 2.** FESEM images of the products as received at different stages: (**a**,**b**) Co(OH)$_2$, (**c**,**d**) Co$_3$O$_4$, and (**e**,**f**) the representative Co/Co$_3$O$_4$@C as treated at 700 °C.

Figure 3 shows the HRTEM images of C-Co-700 sample. The lattice with the distance of 0.24 nm corresponds to the (111) crystal plane of the Co phase. The lattice with the distance of 0.21 nm can be ascribed to the (311) plane of Co$_3$O$_4$. It shows one selected area of electron diffraction pattern, which is indexed to the (311), (440), and (400) planes of Co$_3$O$_4$ and (111) crystal plane of Co, respectively.
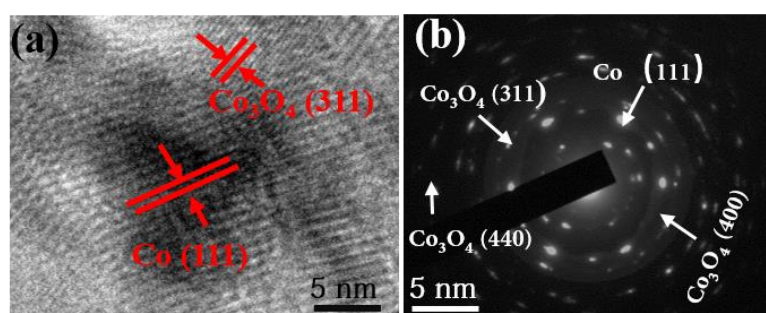

Figure 3. (**a**) HRTEM and (**b**) SAED image of C-Co-700 product.

The crystal structures for Co/Co$_3$O$_4$@C are characterized by X-ray pattern (XRD). As shown in Figure 4a, the diffraction peaks at 36.2° and 42.7° are assigned to the (311) and (400) crystal planes of Co$_3$O$_4$. Besides, other diffraction peaks at 44.2° and 51.1° can be ascribed to the (111) and (200) crystal planes of Co. Furthermore, the intensity of Co signals is gradually stronger as it increases for the product treated with a high temperature, revealing the increased content of Co. As for amorphous carbon shell, there is no obvious signal, because of amorphous state. To confirm existence of carbon, the Raman spectrums are employed here, as plotted in Figure 4b. Clearly, two noticeable peaks at 1360 and 1590 cm^{-1}, representing D and G band, respectively, are found for these Co/Co$_3$O$_4$@C hybrids [24]. It is widely accepted that G band is generated by the graphitized carbon atom which adopts sp^2 hybridized form [25]. D band is induced by the crystal defects or disorders existing in

carbon materials [26]. Commonly, the ratio of D/G band is an indicator of the graphitization degree. In our case, the ratios are estimated to be 0.98, 0.91, and 0.88 for the C-Co-500, C-Co-600, and C-Co-700, respectively. The increased graphitization degree is ascribed to a high carbonization temperature, according to recent achievement [27]. The magnetization loops (M-H) curves were measured by a vibrating sample magnetometer (VSM) (Figure 4c,d). In general, the magnetization value has a vital correlation with permeability parameters, includes real part of permeability and magnetic loss value (μ'/μ''), as can be expressed by the following equations [28]:

$$\mu' = 1 + (M/H)cos\sigma \tag{3}$$

$$\mu'' = (M/H)\,sin\sigma \tag{4}$$

where M represents the magnetization, H means the external magnetic field, and σ refers to the phase lag angle of magnetization behind external magnetic field. From Equations (3) and (4), a high magnetization value is related to a bigger μ' and μ'' values, thus benefiting to the impedance matching and magnetic loss ability. In Figure 4c, the magnetization values are estimated to be 9.0, 33, and 75 emus/g for C-Co-500, C-Co-600, and C-Co-700 samples. The increased magnetization value confirms the enhancement of Co content [29]. The X-ray photoelectron spectrum (XPS) is also performed to analyze the valances of Co. The binding energy values of Co $2p_{3/2}$ are located at 782.1 and 778.2 eV, which can be corresponded to Co_3O_4 and Co, respectively (Figure 4e–g) [30]. The surface area ratio of S_{Co/SCo_3O_4} are 0.23, 0.43, and 0.81 for C-Co-500, C-Co-600, and C-Co-700, respectively, representing the molar ratio.
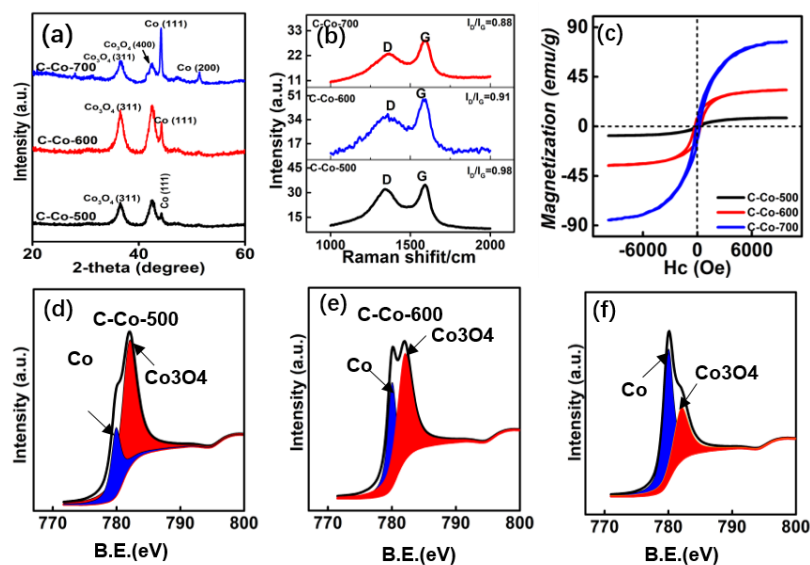

Figure 4. (**a**) XRD patterns, (**b**) Raman spectrum, (**c,d**) *M-H* curves of Co/Co_3O_4@C samples treated at various temperatures, and (**e,f**) XPS spectrums for the Co 3/2 p.

Figure 5 plots the frequency dependence of two-dimensional reflection loss (RL) curves. Considering the transmission line theory, the reflection loss values are calculated using the measured data of relative permittivity and permeability at a given frequency region (2–18 GHz) and thickness layer (1–5 mm). Obviously, the absorption layer filled with Co_3O_4 exhibits the poor EM performance, due to the unqualified RL values (<−10 dB) [31]. But significant improvement can be found for these Co/Co_3O_4@C sample. In fact, a desirable EM absorber is requested to a broadband absorption for the thickness < 2.0 mm. To clarify it, the reflection loss curves at 1.0–2.0 mm are given in Figure 6. In such a thickness region, RL_{min} values of Co_3O_4 are all higher than −2.0 dB, thus cannot be used as absorber. For C-Co-500 product, the minimum RL_{min} value of −10.8 dB is achieved under a thickness of 1.8 mm. In other thickness, there is no frequency region with RL < −10 dB. As the content of Co is increased,

the absorption intensity becomes distinctly stronger. The minimum RL_{min} value can up to -39.4 dB for C-Co-600, while the thickness in only 1.4 mm (Figure 6c). Meanwhile, the qualified frequency region covers 4.3 GHz, ranging from 13.8 to 18.0 GHz. While for C-Co-700 (Figure 6d), the lowest RL_{min} value can be gained is -38.6 dB under a matched thickness of 1.6 mm. The corresponding f_s value is 4.9 GHz. For comparison, the EM performance of Co or C containing hybrids are listed in Table 1, demonstrating that the Co/Co$_3$O$_4$@C hybrids shows improvement of EM absorption ability [32–39].
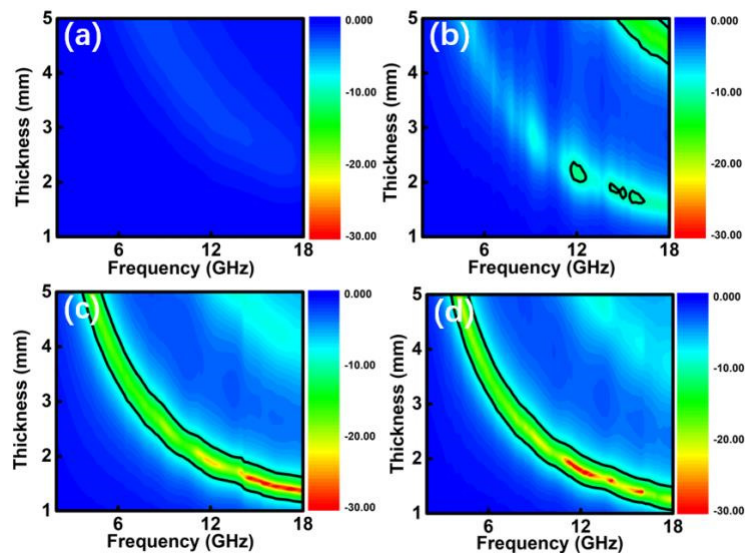

Figure 5. Color-mappings of reflection loss curves for the Co/Co$_3$O$_4$@C and Co$_3$O$_4$ samples: (**a**) Co$_3$O$_4$, (**b**) C-Co-500, (**c**) C-Co-600, and (**d**) C-Co-700.
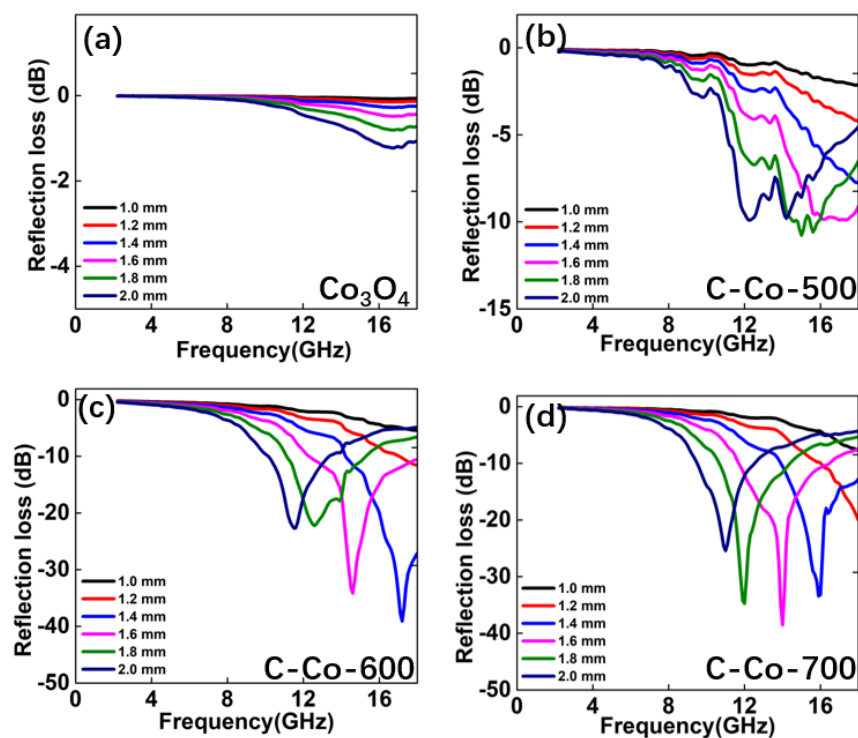
Figure 6. Frequency dependent of reflection loss curves for the Co/Co$_3$O$_4$@C and Co$_3$O$_4$ samples: (**a**) Co$_3$O$_4$, (**b**) C-Co-500, (**c**) C-Co-600, and (**d**) C-Co-700; noted that the thickness < 2.0 mm.

Table 1. Electromagnetic (EM) performances of Co- or C-based hybrids as reported by recent literatures.

Samples	RL_{min} (dB)	Effective Absorption Region (GHz)	Thickness (mm)	Ref.
Co@C	~−10	<3.0	1.5	[32]
Porous carbon	−23.8	~3.8	2.0	[33]
CoO@Co/ZnO/graphene	−51.5	4.7	2.6	[34]
CoNi@C	−24.03	4.32	2.5	[35]
Co/ZnO/C	−52.6	4.9	3.0	[36]
Co_3O_4/graphene	−31.88	3.4	2.0	[37]
Co_3O_4@PANI	−37.39	~4.2	4.0	[38]
Co/CoO	−50 dB	4.2	2.0	[39]
C-Co-600	−39.4 dB	4.3	1.4 mm	This work

It should be noted that EM absorption performance is always determined by the impedance matching and EM attenuation ability. The key factor for the impedance matching ability can be estimated by the ratio of complex permeability/permittivity (μ_r/ε_r) [40]. Figure 7 plots the curves of μ_r, ε_r, and their ratios of μ_r/ε_r. Due to the nonmagnetic characteristic, μ_r of Co_3O_4 is almost a constant of 1.0, according to Figure 7a. ε_r decreases from 4.6 to 4.2. As compared to Co_3O_4, μ_r of C-Co-500 is only a little higher than Co_3O_4, attributing to the low content of Co (Figure 7b). But significant enhancement can be found for ε_r ranging in 7.2~9.9. By further increasing the content of Co, both μ_r and ε_r increase, e.g., μ_r values are ~1.1 and 1.2 for C-Co-600 and C-Co-700, respectively (Figure 7c,d). Meanwhile, ε_r of C-Co-700 is highest and distributed in the region 15.9~12. The ratios of μ_r/ε_r values are then applied to estimate the impedance matching ability (Figure 7e). The ratio of Co_3O_4 is distinct larger than these Co/Co_3O_4@C samples, revealing the good impedance matching behavior. In this case, it can be deduced that the poor EM performance of Co_3O_4 is primarily due to the weaken attenuation ability. For these Co/Co_3O_4@C hybrids, the ratios of C-Co-600 is much closer to C-Co-700, and all are smaller than C-Co-500.
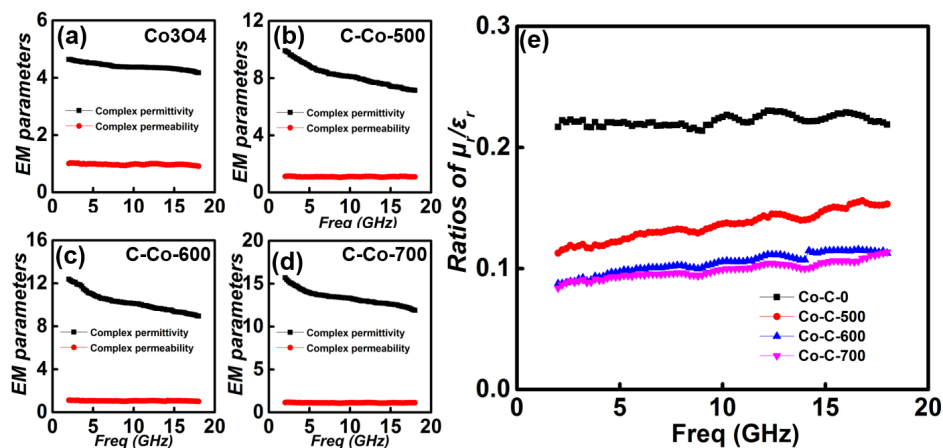

Figure 7. Frequency dependence of μ_r/ε_r curves for the Co/Co_3O_4@C and Co_3O_4 samples: (**a**) Co_3O_4, (**b**) C-Co-500, (**c**) C-Co-600, (**d**) C-Co-700, and (**e**) the ratios of μ_r/ε_r for the Co/Co_3O_4@C and Co_3O_4 sample.

Commonly, the mechanism for EM attenuation results from dielectric and magnetic loss. Figure 8a plots the ε''-f curves for these products. It can be clearly seen that Co_3O_4 achieves the lowest ε'' value (~0.35), representing the worst dielectric loss ability. For Co/Co_3O_4@C samples, the ε'' slowly decreases first as the frequency increases. Then, multiple dielectric loss peaks are observed in high-frequency region (f > 6.5 GHz), revealing polarization relaxation behavior. In such a frequency region (f > GHz), polarization forms primarily included are interfacial and dipole polarization, according to recent discussions on mechanism [41,42]. In general, either dipole or interfacial polarization relaxation

effect can be revealed by the Cole–Cole semicircle. In detail, the relative complex permittivity can be described by the following equations [43–46]:

$$\varepsilon_r = \varepsilon_\infty + \frac{\varepsilon_s - \varepsilon_\infty}{1 + j2\pi f\tau} = \varepsilon' - j\varepsilon'' \tag{5}$$

where ε_s, ε_∞, and τ are static permittivity, relative dielectric permittivity at high-frequency limit, and polarization relaxation time, respectively, whereas, ε' and ε'' can be calculated based on the following equations.

$$\varepsilon' = \varepsilon_\infty + \frac{\varepsilon_s - \varepsilon_\infty}{1 + (2\pi f)^2\tau^2} \tag{6}$$

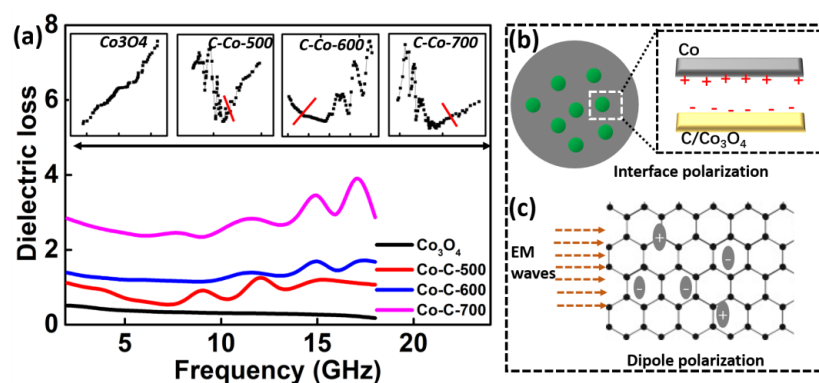$$\varepsilon'' = \frac{2\pi f\tau(\varepsilon_s - \varepsilon_\infty)}{1 + (2\pi f)^2\tau^2} \tag{7}$$

Figure 8. Frequency dependence of dielectric loss curves for the Co/Co$_3$O$_4$@C and Co$_3$O$_4$ samples: the schematic illustration of proposed interface (**b**,**c**) dipole polarization mechanism; noted the inserted images in Figure 8 (**a**) represents the Cole–Cole curves.

Based on Equations (6) and (7), the ε'-ε'' can be expressed as above:

$$(\varepsilon' - \varepsilon_\infty)^2 + (\varepsilon'')^2 = (\varepsilon_s - \varepsilon_\infty)^2 \tag{8}$$

If the plot of ε'-ε'' is a semicircle, it represents one Debye polarization relaxation process which make a contribution for ε''. Commonly, such a semicircle is termed as Cole–Cole semicircle. The inserted images in Figure 8a show the Cole–Cole curves of these products. It can be revealed that only Co/Co$_3$O$_4$@C products exhibit Cole–Cole semicircles, indicating the polarization behavior. The proposed mechanisms for polarization are illustrated in Figure 8b,c. In our case, the developed Co/Co$_3$O$_4$@C exhibits multiple interfaces, including Co/Co$_3$O$_4$, Co/C, and Co$_3$O$_4$/C. When an external EM field is provided, the electrons from the Co will be attracted by Co$_3$O$_4$ or groups of amorphous carbon, because of difference in electronegativity. Consequently, the interfacial relaxation process occurs, favoring the dielectric loss. In addition to interfacial polarization, dipole polarization may also attribute to the dielectric loss value.

Amorphous carbon shell always contains various forms of defects, such as crystal defects, presence of C-containing groups, e.g., –COOH, –C=O, –COH, etc. (Figure 8c). These defects can act as the dipole center and induce dipole polarization. Such a dipole process has a contribution for ε'' [47].

Magnetic loss ability is discussed in Figure 9. Because of the biggest content of Co, C-Co-700 has a largest μ'' value, equaling to 0.24. Meanwhile, μ'' versus frequency exhibits multiple peaks. As we know, μ'' mainly comes from hysteresis loss, domain wall resonance, natural resonance, exchange resonance, and eddy current effect [45]. The hysteresis loss arising from irreversible magnetization is negligible in a weakly applied field, and the domain wall resonance occurs only in multidomain

materials and usually in 1–100 MHz region, and thus, the contributions from hysteresis loss and domain wall resonance to magnetic loss can be excluded in our material system. If the magnetic loss originates from eddy current effect, the values of $C_0 (C_0 = \mu''(\mu')^{-2}f^{-1} = 2\pi\mu_0\sigma d^2/3)$ should be a constant when the frequency increases [48,49]. The C_0 values of all samples fluctuate at full frequency region (Figure 9b). Hence, we can deduce that the magnetic loss mainly results from natural resonance and exchange resonances.
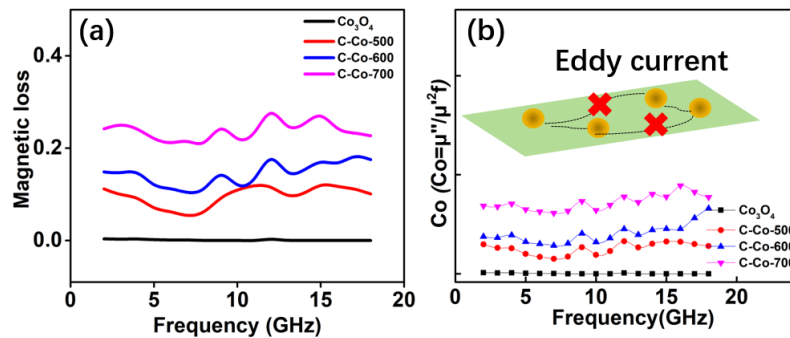

Figure 9. (**a**) Frequency dependence of magnetic loss curves for the $Co/Co_3O_4@C$ and Co_3O_4 samples and (**b**) the Co-f curves of the four products.

The attenuation constant α represents the integral loss ability, including magnetic or dielectric loss, which can be calculated by following equation [50]:

$$\alpha = \frac{\sqrt{2}\pi f}{c} \times \sqrt{(\mu''\varepsilon'' - \mu'\varepsilon') + \sqrt{(\mu''\varepsilon'' - \mu'\varepsilon')^2 + (\mu'\varepsilon'' + \mu''\varepsilon')^2}} \qquad (9)$$

From Figures 8 and 9, we can find that C-Co-700 sample has the highest dielectric and magnetic losses, thus leading to a biggest attenuation constant α (Figure 10). The content of Co plays a key role on tuning the dielectric and magnetic loss ability. It also has proven that Co_3O_4 has a quite lower attenuation constant α. Overall, C-Co-600 achieves the best EM performance which attributes to the several factors. First, the Co/Co_3O_4 as the core has efficiently prevented the eddy current effect. Second, the suitable component of Co ensures the strong interfacial polarization, which is beneficial to dielectric loss. In addition, a suitable content of Co also maintains a moderately ε_r value, hence enabling to balance the impedance matching ability.
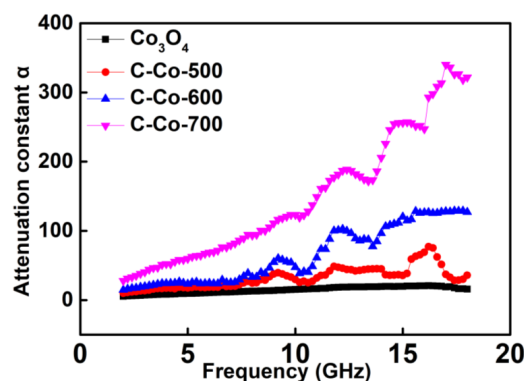

Figure 10. Wave-attenuation constant α for these products.

4. Conclusions

In this work, a $Co/Co_3O_4@C$ product was developed by a facile hydrothermal and annealing method. First, the spherical-shaped Co_3O_4 with an average size of ~400 nm was prepared and then coated by carbon. The as-obtained $Co_3O_4@C$ was heated at various temperatures, resulting in

Co/Co$_3$O$_4$@C hybrids. The content of Co was tunable by only controlling the temperatures. The EM performance were studied, based on the transmission line theory. The minimum reflection loss value (RL$_{min}$) of −39.4 dB could be achieved for the Co/Co$_3$O$_4$@C sample. The corresponding thickness was only 1.4 mm. Furthermore, the frequency region with *RL* < −10 dB, was up to 4.3 GHz, covering 13.7~18.0 GHz. The excellent electromagnetic absorption mechanism was discussed in depth, which was attributed to the multi-interface-induced interface polarization. Meanwhile, the existed magnetic Co enabled balancing the impedance matching behavior.

References

1.　Xu, Y.; Yang, Y.; Yan, D.; Duan, H.; Zhao, G.; Liu, Y. Gradient Structure Design of Flexible Waterborne Polyurethane Conductive Films for Ultraefficient Electromagnetic Shielding with Low Reflection Characteristic. *ACS Appl. Mater. Interfaces* **2018**, *10*, 19143–19152. [CrossRef]

2.　Pastore, R.; Delfini, A.; Micheli, D.; Vricella, A.; Marchetti, M.; Santoni, F.; Piergentili, F. Carbon foam electromagnetic mm-wave absorption in reverberation chamber. *Carbon* **2019**, *144*, 63–71. [CrossRef]

3.　Lv, H.; Yang, Z.; Xu, H.B.; Wang, L.Y.; Wu, R.B. An electrical switch-driven flexible electromagnetic absorber. *Adv. Funct. Mater.* **2019**, *30*, 1907251. [CrossRef]

4.　Lou, Z.C.; Yaun, C.L.; Zhang, Y.; Li, Y.; Cai, J.B.; Yang, L.T.; Wang, W.K.; Han, H.; Zou, J. Synthesis of porous carbon matrix with inlaid Fe$_3$C/Fe$_3$O$_4$ microparticles as an effective electromagnetic absorber from natural wood shavings. *J. Alloys Compd.* **2019**, *775*, 800–809. [CrossRef]

5.　Feng, A.; Hou, T.; Jia, Z. Synthesis of a hierarchical carbon fiber@cobalt ferrite@manganese dioxide composite and its application as a microwave absorber. *RSC Adv.* **2020**, *10*, 10501. [CrossRef]

6.　Zhou, X.F.; Jia, Z.R.; Kou, J.H.; Cao, H.J.; Liu, X.H. Construction of multiple electromagnetic loss mechanism for enhanced electromagnetic absorption performance of fish scale-derived biomass absorber. *Compos. Part B-Eng.* **2020**, *192*, 107980. [CrossRef]

7.　Lou, Z.; Li, R.; Wang, P.; Zhang, Y.; Chen, B.; Huang, C.; Wang, C.; Han, H.; Li, Y. Phenolic foam-derived magnetic carbon foams (MCFs) with tunable electromagnetic wave absorption behavior. *Chem. Eng. J.* **2019**. [CrossRef]

8.　Zhang, Y.; Huang, Y.; Zhang, T.F.; Chang, H.C.; Xiao, P.S.; Chen, H.H.; Huang, Z.Y.; Chen, Y.S. Broadband and tunable high-performance microwave absorption of an ultralight and highly compressible graphene foam. *Adv. Mater.* **2015**, *27*, 2049–2053. [CrossRef]

9.　Lim, H.R.; Jung, S.J.; Hwang, T.Y.; Lee, J.M.; Kim, K.H.; Cho, H.B.; Choa, Y.H. Electromagnetic wave absorption properties of Fe/MgO composites synthesized by a simple ultrasonic spray pyrolysis method. *Appl. Surf. Sci.* **2019**, *473*, 1009–1013. [CrossRef]

10.　Lv, H.; Zhang, H.Q.; Zhao, J.; Ji, G.; Du, Y.W. Achieving excellent bandwidth absorption by a mirror growth process of magnetic porous polyhedron structures. *Nano Res.* **2016**, *9*, 1813–1822. [CrossRef]

11.　Lu, Y.Y.; Wang, Y.T.; Li, H.L.; Lin, Y.; Jiang, Z.Y.; Xie, Z.X.; Kuang, Q.; Zheng, L.S. MOF-derived porous Co/C nanocomposites with excellent electromagnetic wave absorption properties. *ACS Appl. Mater. Interface* **2015**, *7*, 13604–13611. [CrossRef] [PubMed]

12.　Wu, G.; Zhang, H.X.; Luo, X.X.; Yang, L.J. Investigation and optimization of Fe/ZnFe$_2$O$_4$ as a wide-band electromagnetic absorber. *J. Colloid Interf. Sci.* **2019**, *536*, 548–555. [CrossRef] [PubMed]

13. Zhao, B.; Li, Y.; Liu, J.W.; Fan, L.; Gao, K.; Bai, Z.Y.; Liang, L.Y.; Gao, X.Q.; Zhang, R. Symmetrical polyhedron-bowl Co/CoO with hexagonal plate to forward electromagnetic wave absorption ability. *CrystEngComm* **2019**, *5*, 816–826. [CrossRef]

14. Li, S.P.; Huang, Y.; Zhang, N.; Zong, M.; Liu, P.B. Synthesis of polypyrrole decorated FeCo@SiO$_2$ as a high-performance electromagnetic absorption material. *J. Alloys Compd.* **2019**, *774*, 532–539. [CrossRef]

15. Xu, Z.; Du, Y.C.; Liu, D.W.; Wang, Y.H.; Ma, W.J.; Wang, Y.; Xu, P.; Han, X.J. Pea-like Fe/Fe$_3$C nanoparticles embedded in Nitrogen-doped carbon nanotubes with tunable dielectric/magnetic loss and efficient electromagnetic absorption. *ACS Appl. Mater. Interfaces* **2019**, *11*, 4268–4277. [CrossRef]

16. Chen, C.; Zhen, S.; Zhang, B.S.; Zhou, Y.Y.; Li, S.M. Development of sulfide-doped graphene/Fe$_3$O$_4$ absorber with wide band electromagnetic absorption performance. *J. Alloys Compd.* **2019**, *770*, 90–97. [CrossRef]

17. Huangfu, Y.M.; Liang, C.B.; Han, Y.X.; Qiu, H.; Song, P.; Wang, L.; Kong, J.; Gu, J.W. Fabrication and investigation on the Fe3O4/thermally annealed graphene aerogel/epoxy electromagnetic interference shielding nanocomposites. *Compos. Sci. Technol.* **2019**, *169*, 70–75. [CrossRef]

18. Lv, H.L.; Guo, Y.H.; Wu, G.L.; Ji, G.B.; Zhao, Y.; Xu, Z.C.J. Interface polarization strategy to solve electromagnetic interference issue. *ACS Appl. Mater. Interfaces.* **2017**, *9*, 5660–5668. [CrossRef]

19. Ma, J.R.; Shu, J.C.; Cao, W.Q.; Zhang, M.; Wang, X.X.; Yuan, J.; Cao, M.S. A green fabrication and variable temperature electromagnetic properties for thermal stable microwave absorption towards flower-like Co$_3$O$_4$@rGO/SiO$_2$ composites. *Compos. Part B-Eng.* **2019**, *166*, 187–195. [CrossRef]

20. Zhang, M.; Li, Z.J.; Wang, T.; Ding, S.Q.; Song, G.Y.; Zhao, J.; Meng, A.; Yu, H.Y.; Li, Q.D. Preparation and electromagnetic wave absorption performance of Fe$_3$Si@SiC@SiO$_2$ nanocomposites. *Chem. Eng. J.* **2019**, *362*, 619–627. [CrossRef]

21. Lv, H.; Ji, G.; Liu, W.; Du, Y.W.Y. Achieving hierarchical hollow carbon@Fe@Fe3O4 nanospheres with superior microwave absorption properties and lightweight features. *J. Mater. Chem. C* **2015**, *3*, 10232–10241. [CrossRef]

22. Liang, X.; Cheng, Y.; Zhang, H. Coin-like α-Fe$_2$O$_3$@CoFe$_2$O$_4$ core-shell composites with excellent electromagnetic absorption performance. *ACS Appl. Mater. Interfaces.* **2015**, *7*, 4744–4750.

23. Yang, Z.; Ong, S.J.H.; Wei, C.; Liao, H.; Xi, S.B.; Du, Y.H. A flexible microwave shield with tunable frequency-transmission and electromagnetic compatibility. *Adv. Funct. Mater.* **2019**, *29*, 1900163.

24. Yang, L.J.; Zhang, Y.; Liu, J.C.; Yang, Z.H. Multiple polarization effect of shell evolution on hierarchical hollow C@MnO$_2$ composites and their wideband electromagnetic wave absorption properties. *Chem. Eng. J.* **2020**, *392*, 123666. [CrossRef]

25. Zhang, H.X.; Jia, Z.; Feng, A.; Zhou, Z.H.; Zhang, C.H.; Wang, K.K.; Liu, N. Enhanced microwave absorption performance of sulfur-doped hollow carbon microspheres with mesoporous shell as broadband absorber. *Compos. Commun.* **2020**, *19*, 42–50. [CrossRef]

26. Lv, H.; Yang, Z.; Wang, P.L.Y.; Ji, G.; Song, J.Z.; Zheng, L.R. A voltage-boosting strategy enabling a low-frequency, flexible electromagnetic wave absorption device. *Adv. Mater.* **2018**, *30*, 1706343. [CrossRef]

27. Kong, L.; Yin, X.W.; Xu, H.L.; Yuan, X.Y.; Wang, T.; Xu, Z.W.; Huang, J.F.; Yang, R.; Fan, H. Powerful absorbing and lightweight electromagnetic shielding CNTs/RGO composite. *Carbon* **2019**, *145*, 61–66. [CrossRef]

28. Wu, G.L.; Cheng, Y.H.; Yang, Z.H.; Jia, Z.R.; Wu, H.J.; Yang, L.J.; Li, H.L.; Guo, P.Z. Design of carbon sphere/magnetic quantum dots with tunable phase compositions and boost loss behavior. *Chem. Eng. J.* **2018**, *333*, 519–528. [CrossRef]

29. Li, W.C.; Cai, H.W.; Kang, Y.; Ying, Y.; Yu, J.; Zheng, J.W.; Qiao, L.; Jiang, Y.; Che, S.L. High permeability and low loss bioinspired soft magnetic composites with nacre-like structure for high frequency applications. *Acta Mater.* **2019**, *167*, 267–274. [CrossRef]

30. Li, J.; Zhao, X.L.; Liu, J.P.; Zhang, L.; Yang, C.H. Ultralight carbon-based Co(OH)$_2$-Co$_3$O$_4$/nanocomposite with superior performance in wave absorption. *J. Alloys Compd.* **2019**, *777*, 954–962. [CrossRef]

31. Zhao, B.; Guo, X.Q.; Zhao, W.Y.; Deng, J.S.; Fan, B.B.; Shao, G.; Bai, Z.Y.; Zhang, R. Facile synthesis of yolk-shell Ni@void@SnO$_2$(Ni$_3$Sn$_2$) ternary composites via galvanic replacement/Kirkendall effect and their enhanced microwave absorption properties. *Nano Res.* **2017**, *10*, 331–343. [CrossRef]

32. Wu, N.N.; Qiao, J.; Liu, J.R.; Du, W.J.; Xu, D.M.; Liu, W. Strengthened electromagnetic absorption performance derived from synergistic effect of carbon nanotube hybrid with Co@C beads. *Adv. Compos. Mater.* **2018**, *1*, 149–159. [CrossRef]

33. Zhao, B.; Deng, J.S.; Liang, L.Y.; Zuo, C.Y.X.; Bai, Z.Y.; Guo, X.Q.; Zhang, R. Lightweight porous Co$_3$O$_4$ and Co/CoO nanofibers with tunable impedance match configuration-dependent microwave absorption properties. *CrystEngComm* **2017**, *41*, 6095–6106. [CrossRef]

34. Zhu, C.L.; Zhang, S.; Sun, Y.; Chen, Y.J. Incorporation of CoO@Co yolk-shell nanoparticles and ZnO nanoparticles with graphene sheets as lightweight and high-performance electromagnetic wave absorbing material. *J. Alloys Compd.* **2017**, *711*, 552–559. [CrossRef]

35. Zhang, X.; Yan, F.; Zhang, S.; Yuan, H.R.; Zhu, C.L.; Zhang, X.T.; Chen, Y.J. Hollow N-doped carbon polyhedron containing CoNi alloy nanoparticles embedded within few-layer N-doped graphene as high-performance electromagnetic wave absorbing material. *ACS Appl. Mater. Interfaces* **2018**, *10*, 24920–24929. [CrossRef] [PubMed]

36. Liao, Q.; He, M.; Zhou, Y.M.; Nie, S.X.; Wang, Y.J.; Hu, S.C.; Yang, H.Y.; Li, J.F.; Tong, Y. Highly cuboid-shaped heterobimetallic metal-organic frameworks derived from porous Co/ZnO/C microrods with improved electromagnetic wave absorption capabilities. *ACS Appl. Mater. Interfaces* **2018**, *10*, 29136–29144. [CrossRef] [PubMed]

37. Li, Y.; Li, S.; Zhang, T.; Shi, L.L.; Liu, S.T.; Zhao, Y. 3D hierarchical Co$_3$O$_4$/reduced graphene oxide/melamine derived carbon foam as a comprehensive microwave absorbing material. *J. Alloys Compd.* **2019**, *792*, 424–431. [CrossRef]

38. Jia, H.X.; Xing, H.L.; Ji, X.L.; Gao, S.T. Synergistic effect of hexagonal flake Co$_3$O$_4$@PANI core-shell composites with excellent microwave absorbing properties. *J. Mater. Sci. Mater. Electron.* **2019**, *30*, 3386–3395. [CrossRef]

39. Liang, X.H.; Ji, G.B.; Zhang, H.Q.; Du, Y.W. Porous three-dimensional flower-like Co/CoO and excellent electromagnetic absorption properties. *ACS Appl. Mater. Interfaces* **2015**, *7*, 9776–9783.

40. Liu, H.H.; Li, Y.J.; Yuan, M.W.; Sun, G.B.; Li, H.F.; Ma, S.M.; Liao, Q.L.; Zhang, Y. In-situ preparation of cobalt nanoparticles decorated in N-doped carbon nanofibers as excellent electromagnetic wave absorbers. *ACS Appl. Mater. Interfaces* **2018**, *10*, 22591–22601. [CrossRef]

41. Dong, S.; Zhang, X.H.; Hu, P.T.; Zhang, W.Z.; Han, J.C.; Hu, P. Biomass-derived carbon and polypyrrole addition on SiC whiskers for enhancement of electromagnetic wave absorption. *Carbon* **2019**, *359*, 882–893. [CrossRef]

42. Liu, L.; He, N.; Wu, T.; Hu, P.B.; Tong, G.X. Co/C/Fe/C hierarchical flowers with strawberry-like surface as surface plasmon for enhanced permittivity, permeability, and microwave absorption properties. *Chem. Eng. J.* **2019**, *355*, 103–108. [CrossRef]

43. Yang, M.L.; Yuan, Y.; Yin, W.L.; Peng, Q.Y.; Li, J.J.; He, X.D. Co/CoO@C nanocomposites with a hierarchical bowknot-like nanostructure for high-performance broadband electromagnetic wave absorption. *Appl. Surf. Sci.* **2019**, *469*, 607–616. [CrossRef]

44. Wu, G.; Jia, Z.; Zhou, X.F.; Nie, G. Interlayer controlled of hierarchical MWCNTs@C@Fe$_x$O$_y$ cross-linked composite with wideband electromagnetic absorption performance. *Compos. Part A-Appl. Sci. Manuf.* **2020**, *128*, 105687. [CrossRef]

45. Lv, H.; Zhang, H.; Ji, G. Interface strategy to achieve tunable high frequency attenuation. *ACS Appl. Mater. Interfaces* **2016**, *8*, 6295–6538. [CrossRef] [PubMed]

46. Sheng, A.; Ren, W.; Yang, Y.; Yan, D.X.; Duan, H.; Zhao, G.; Liu, Y.; Li, Z.M. Multilayer WPU conductive composites with controllable electro-magnetic gradient for absorption-dominated electromagnetic interference shielding. *Compos. Part A* **2020**, *129*, 105692. [CrossRef]

47. Liu, X.F.; Nie, X.Y.; Yu, R.H.; Feng, H.B. Design of dual-frequency electromagnetic wave absorption by interface modulation strategy. *Chem. Eng. J.* **2018**, *334*, 153–161. [CrossRef]

48. Guo, Y.H.; Yang, Z.; Zhao, Y. A brief introduction to the fabrication and synthesis of graphene based composites for the realization of electromagnetic absorbing materials. *J. Mater. Chem. C* **2017**, *3*, 491–512.

49. Li, J.S.; Xie, Y.Z.; Lu, W.B.; Chou, T.W. Flexible electromagnetic wave absorbing composite based on 3D rGO-CNT-Fe$_3$O$_4$ ternary films. *Carbon* **2018**, *129*, 76–84. [CrossRef]

50. Jia, Z.; Kou, K.; Yin, S.; Feng, A. Magnetic Fe nanoparticle to decorate N dotted C as an exceptionally absorption-dominate electromagnetic shielding material. *Compos. Part B-Eng.* **2020**, *189*, 107895. [CrossRef]